DIRECT NUMERICAL SIMULATION OF 3-D HYPERSONIC BOUNDARY LAYER RECEPTIVITY TO FREESTREAM DISTURBANCES

Xiaolin Zhong *
University of California, Los Angeles, California 90095

Abstract

In direct numerical simulation (DNS) of the receptivity to freestream disturbances and the laminar-turbulent transition process of hypersonic boundary layers, it is necessary to consider the effect of the interaction between the bow shocks and wave fields. In previous papers, we developed a fifth-order shock-fitting numerical method and conducted the DNS of the generation of boundary layer instability waves due to freestream acoustic disturbances for a 2-D Mach 15 flow over a parabolic leading edge. It was shown that instability waves developed in hypersonic boundary layers behind bow shocks contain both the first and second mode waves. The use of the high-order shock fitting scheme makes it possible to accurately simulate physical bow-shock oscillations and interactions. This paper extends the previous 2-D work to a 3-D shock-fitting scheme for the DNS of 3-D hypersonic flows over blunt cones of arbitrary cross sections and over blunt wedges. The new 3-D shock-fitting scheme is then used to study the receptivity of both axisymmetric and 3-D hypersonic boundary layers to freestream disturbances in Mach 15 flows over a parabolic cone and a parabolic wedge. The receptivity characteristics of axisymmetric and planar hypersonic boundary layers over blunt bodies are compared.

Introduction

The prediction of laminar-turbulent transition in hypersonic boundary layers is a critical part of the aerodynamic design and control of hypersonic vehicles [1]. In general, the transition is a result of nonlinear response of the laminar boundary layers to forcing disturbances [2]. In an environment with small initial disturbances, the path to transition consists of three stages: 1) receptivity, 2) linear eigenmode growth or transient growth, and 3) nonlinear breakdown to turbulence.

The receptivity [3] of boundary layers to disturbances is the process of converting environmental disturbances into instability waves in the boundary layers. The receptivity mechanism provides important initial conditions in terms of amplitude, frequency, and phase for the instability waves in the boundary layers. The past theoretical, experimental, and numerical studies of boundary-layer receptivity were reviewed by Goldstein and Hultgren [4] and by Saric, Reed, and Kerschen [5]. Most theoretical results on incompressible boundary-layer receptivity have been obtained from the asymptotic analysis [6]. The asymptotic analysis explains how the long wavelength freestream acoustic disturbances enter a boundary layer and generate short-wavelength Tollmien-Schlichting (T-S) waves downstream of the leading edge. Recently, direct numerical simulation of the Navier-Stokes equations has become a powerful tool in the studies of stability and transition [7–9]. Examples of the DNS studies on the receptivity of low-speed boundary layers can be found in Refs. [10–17].

For hypersonic flow over blunt bodies, the receptivity phenomena are more complex than those in low-speed flow regimes [18,19]. The receptivity and transition of hypersonic boundary layers over blunt bodies are altered considerably by the presence of the bow shocks which are located very close to body surfaces at hypersonic Mach numbers. For the receptivity to freestream disturbances, irrespective of the nature of the freestream disturbance waves, the interaction with bow shocks always generates all three types of acoustic, entropy, and vorticity waves. These transmitted waves are propagated downstream and interact with the boundary layers on the body surfaces. At the same time, boundary layers also generate reflected acoustic waves impinging on the shocks from behind which generates further disturbances to the shocks and wave fields. Figure 1 shows a schematic of the wave field interactions near a hypersonic leading edge affected by freestream disturbances. Furthermore, stability and transition of hypersonic boundary layers are affected by nose bluntness and by the boundary-layer swallowing of entropy layers created by bow shocks [20–22].

Therefore, for the numerical simulation of hypersonic boundary-layer transition, it is necessary to include the effect of bow shocks and nose bluntness. High-order accurate numerical methods are required in the direct numerical simulation in order to resolve all relevant flow time and length scales related to the instability waves. Conventional high-order schemes, however, can only be used in flow fields without shock waves. Though nonlinear shock capturing schemes, such as the TVD and

*Associate Professor, Mechanical and Aerospace Engineering Department, e-mail: xiaolin@seas.ucla.edu, Member AIAA.

ENO schemes, have been very successful in compute aerodynamic properties of hypersonic flows with shock waves, the shock capturing methods are often not accurate enough to accurately compute physical curved bow shock oscillations and shock interactions with short-length-scale instability waves [23].

In order to simulate hypersonic boundary-layer receptivity, stability, and transition with strong bow shocks, we [24] developed and validated a set of fifth and seventh-order shock-fitting schemes for the DNS of practical hypersonic flows over blunt bodies. The use of shock-fitting method makes it possible to accurately compute the physical bow-shock interactions, and the development of instability waves in the boundary layers. Subsequently, we [17] used the new schemes to conduct DNS studies of the receptivity of a hypersonic boundary layer to 2-D freestream monochromatic planar acoustic disturbances for a Mach 15 flow over a parabolic leading edge. Local parallel linear stability analysis (LST) of the stability of the hypersonic boundary layer over the blunt wedge was also conducted [25] to compare with DNS results and to identify instability modes obtained by the DNS studies. Numerical accuracy of the DNS results for such hypersonic boundary layer receptivity was evaluated by grid refinement studies and by comparison with other experimental and theoretical results. These 2-D studies showed that instability waves developed in the hypersonic boundary layer behind the bow shock contain both the first and second mode [26] instabilities. The size and the strength of the two regions depend on the frequency of the disturbances. The results also indicated that external disturbances, especially the entropy and vorticity ones, enter the boundary layer mainly in the leading edge region to generate instability waves.

The objective of this paper is extend the previous 2-D high-order shock-fitting schemes in [17, 24] to the DNS of 3-D hypersonic boundary layers over blunt bodies of arbitrary cross sections. The numerical methods for spatial discretization of the 3-D full Navier-Stokes equations are a fifth-order shock-fitting scheme in streamwise and wall-normal directions, and a Fourier collocation method in the periodic spanwise flow direction for the case of a wedge geometry or in the azimuthal direction for the case of a cone geometry. The spatially discretized equations are advanced in time using a Low-Storage Runge-Kutta scheme of Williamson [27] of up to the third order. The new 3-D schemes are then used to study the receptivity of an axisymmetric hypersonic boundary layer over an axisymmetric parabolic cone. The disturbances are freestream weak monochromatic planar acoustic waves. The axisymmetric receptivity results are compared with the corresponding planar 2-D results reported in [17]. The new 3-D schemes are also applied to the receptivity of a 2-D hypersonic boundary mean flow over a blunt wedge to 3-D oblique free stream disturbances. For this case, the mean flow is 2-D but the unsteady flow fields are 3-D.

Equations and Numerical Methods

The governing equations and numerical methods are briefly summerized here. Details can be found in previous papers for 2-D flows [17, 24]. The governing equations are the unsteady full three-dimensional Navier-Stokes equations in the conservation-law form:

$$\frac{\partial U^*}{\partial t^*} + \frac{\partial F^*{}_j}{\partial x_j^*} + \frac{\partial F^*{}_{vj}}{\partial x_j^*} = 0 \qquad (1)$$

where superscript "$*$" represents dimensional variables, and

$$U^* = \{\rho^*, \rho^* u_1^*, \rho^* u_2^*, \rho^* u_3^*, e^*\} \qquad (2)$$

The gas is assumed to be thermally and calorically perfect. The viscosity and heat conductivity coefficients are calculated using the Sutherland's law together with a constant Prandtl number Pr.

We nondimensionalize the velocities with respect to the freestream velocity U_∞^*, length scales with respect to a reference length d^* given by the body surface equation, density with respect to ρ_∞^*, pressure with respect to p_∞^*, temperature with respect to T_∞^*, time with respect to d^*/U_∞^*, vorticity with respect to U_∞^*/d^*, entropy with respect to C_p^*, wave number with respect to $1/d^*$, etc. The dimensionless flow variables are denoted by the same dimensional notation but without the superscript "$*$".

Receptivity Simulations

The numerical simulation for the receptivity of hypersonic flows over a blunt cone or a blunt wedge is carried out using the new 3-D fifth-order shock fitting scheme where the outer grid line is the bow shock. Figure 2 shows a schematic of the general 3-D shock fitted grids used for case of flow over a blunt wedge. Shock fitting grids for hypersonic flow over a blunt cone are generated similarly. The grids are stretched in both streamwise and wall-normal directions. The unsteady bow shock shape and shock oscillations are solved as part of the computation solutions. Analytical formulas of the metric coefficients for coordinates transformation are used to ensure numerical accuracy for the unsteady coordinate transformation in the simulations.

In the simulations, steady flow solutions are first obtained by advancing the unsteady flow computations to convergence using the fifth-order computer code. No disturbances are imposed in the freestream. The steady shock shape is obtained as a part of the numerical solutions. Subsequently, unsteady viscous flows are computed by imposing a continuous planar acoustic single-frequency disturbance wave on the steady flow variables at the freestream side of the bow shock. The shock/disturbance interactions and generation of T-S waves in the boundary layer are solved using the nonlinear Rankine-Hugoniot relations at the shock and the

full Navier-Stokes equations in the flow fields. The unsteady calculations are carried out for about 15 to 30 periods in time until the unsteady solutions reach a time periodic state. Finally, the unsteady computations are carried out for additional periods in time to perform FFT on the perturbation field to obtain the Fourier amplitudes and phase angles for the perturbations of the unsteady flow variables in the flow field.

The freestream disturbances are assumed to be weak monochromatic planar acoustic waves with wave front oblique to the center line of the body in the $x-z$ plane at an angle of ψ. The perturbations of flow variables in the freestream introduced by the freestream acoustic wave before reaching the bow shock can be written in the following form:

$$q'_\infty = |q'|_\infty e^{i(k\cos\psi\, x + k\sin\psi\, z - \omega t)} \qquad (3)$$

where $|q'|$ represents one of the flow variables, $|u'|$, $|v'|$, $|w'|$, $|p'|$, and $|\rho'|$. The freestream perturbation amplitudes satisfy the following relations:

$$|u'|_\infty = \epsilon\cos\psi\,, \qquad |v'|_\infty = 0\,,$$
$$|p'|_\infty = \gamma M_\infty \epsilon\,, \qquad |\rho'|_\infty = M_\infty \epsilon$$
$$|w'|_\infty = \epsilon\sin\psi$$

where ϵ represents the freestream wave magnitude. The angle ψ is the angle of freestream wave with respect to the x axis in the x-z plane, where $\psi = 0$ corresponds to 2-D planar waves. The parameter k is the dimensionless freestream wave number which is related to the dimensionless circular frequency ω by:

$$\omega = k\,(\cos\psi + M_\infty^{-1}) \qquad (4)$$

The dimensionless frequency F is defined as:

$$F = \frac{\omega^* \nu^*}{U_\infty^{*2}}\,. \qquad (5)$$

The numerical method has been tested and validated in [24]. For the current receptivity computations, grid refinements are used to ensure that both steady and unsteady solutions are grid independent. In addition, the direct simulation of the development of instability waves along the boundary layer is carried out in successive computational zones from the leading edge to downstream. The development of instability waves in Zone 1 is first computed until the solutions reach a time periodic state. Having finished the simulation in Zone 1, the simulations in Zone 2 are carried out using the solutions from Zone 1 as boundary conditions at the inlet. The use of multi-zone approach provides a way to evaluate the magnitudes of possible numerical wave reflection at the exit boundary. If there is no spurious numerical reflection at the exit boundary, the solutions from the two zones in the overlap region are the same. The comparison of the results in the overlap region shows that the wave reflections at the exit boundary for the present test cases are negligible or are limited to very small amplitudes near the exit of Zone 1.

Receptivity of Axisymmetric Hypersonic Flow

The first case is the receptivity of an axisymmetric boundary layer to weak freestream acoustic disturbance waves for a Mach 15 hypersonic flow past a parabolic blunt cone at zero angle of attack. In order to compare the receptivity results of axisymmetric and planar hypersonic flows, the axisymmetric flow conditions and the parabolic geometry are chosen to be the same as those for the planar 2-D cases presented in [17]. Specifically, the body surface is a parabolic cone given by:

$$x^* = a^* z^{*2} + b^* y^{*2} - d^* \qquad (6)$$

where a^*, b^*, and d^* are constants, and d^* is used as the reference length. In the present simulations, the cone has an axisymmetric shape with a circular cross section by specifying $a^* = b^*$. The flow conditions are

$M_\infty = 15$ $\qquad$ $\epsilon = 5 \times 10^{-4}$
$T^*_\infty = 192.989\,K$ $\qquad$ $p^*_\infty = 10.3\,Pa$
$T^*_w = 1000\,K$ $\qquad$ $\gamma = 1.4$
$R^* = 286.94\,Nm/kgK$ $\qquad$ $Pr = 0.72$
$a^* = b^* = 40\,m^{-1}$ $\qquad$ $d^* = 0.1\,m$
$T^*_r = 288\,K$ $\qquad$ $T^*_s = 110.33\,K$
$\mu^* = 0.17894 \times 10^{-4} kg/ms$
Nose Radius of Curvature $= r^* = 0.0125\,m$
$Re_\infty = \rho^*_\infty U^*_\infty d^*/\bar{\mu}^*_\infty = 6026.55$

The body surface is assumed to be a non-slip wall with an isothermal wall temperature T^*_w. So far, only one test case with dimensionless frequency of the disturbance wave $F = 1770$ has been computed and is presented in this paper.

Though the flow is axisymmetric, the acutal computations are obtained for 3-D flow fields without the axisymmetric assumption. We choose such approach because the main purpose of our study is the DNS of general 3-D transient hypersonic flows. The present axisymmetric flow computations serve as a first test case for the new general 3-D code. The results presented in this paper are obtained using 80 grid points in the streamwise direction and 60 points in the wall-normal direction. Since the flow is axisymmetric, only 4 Fourier collocation points are needed in computing the azimuthal direction. Figure 3 shows the steady solution for a set of $80 \times 60 \times 32$ computational grid obtained by the simulation. The axisymmetric steady solutions for velocity vectors are shown in Fig. 4. The bow shock and development of boundary layers along the body surface are shown in this figure. Figure 5 shows the unsteady instantaneous perturbations of the velocity velocity vectors for the receptivity of the axisymmetric Mach 15 flow over the parabolic cone with zero angle of attack. Both steady and unsteady bow shocks are captured well by the methods. Since these steady and unsteady flows are axisymmetric, we will present the results only in a computational surface of a fixed azimuthal angle in the following sections.

Steady Flow Solutions

Figure 7 shows the contours of steady axisymmetric flow solutions of Mach numbers, pressure, and entropy for the Mach 15 flow over the cone. Compared with the corresponding planar 2-D flow over a parabolic leading edge [17], the bow shock in the axisymmetric flow is located much closer to the body surface because of the 3-D effect. Consequently, the Mach numbers behind the shock for the axisymmetric case are larger than those for the corresponding planar case. The high Mach numbers in general lead to more stable boundary layers at hypersonic flow regime. Meanwhile, the entropy contours show an entropy layer which is generated by the bow shock. The swallowing of the entropy layer by the boundary layer has been shown to play an important role in the stability and transition of the boundary layer downstream [20]. The entropy layer for the axisymmetric case is closer to the body surface than the planar case.

More quantitative pictures of the axisymmetric mean flow over the cone are shown in Fig. 8 for the pressure, temperature, and velocities profiles along a range of wall-normal grid lines. The x coordinates of the intersecting points of these wall-normal grid lines on the surface are listed in Table 1. Similar to the planar case, the axisymmetric flow has a favorable pressure gradient along the body surface. The pressure difference between those behind the shock and on the body surface is shown in Fig. 6. The axisymmetric flow has much more uniform pressure across the boundary layers at downstream locations. In addition, the tangential velocity (u_t) profiles along the wall-normal direction are much fuller than the corresponding planar flow results. The normal velocity components (u_n) are much smaller than the planar results. In the planar case, u_n is about 10% of the tangential velocity u_t due to curvature effect as compared to less than 5% for the axisymmetric flow.

Table 1. x coordinates of wall-normal grid lines.

Index i	x_s Coordinates
25	-0.756873
35	-0.557069
45	-0.297524
55	0.0376505
65	0.465454
75	1.00326

For compressible boundary layers over flat plates, Lin and Lees [28] showed that a generalized inflection point for inviscid instability corresponds to the zeros of $d(\rho du/dy_n)/dy$. For the planar 2-D hypersonic flow over a parabola, there is a generalized inflection point in the boundary layer [17]. This generalized inflection point moves away from the wall as x increases. Figure 9 shows the variation of axisymmetric $\rho(du_t/dy_n)$ along grid lines normal to parabola surface. For the boundary layer in the axisymmetric flow, on the other hand, the generalized inflection point is not present near the leading edge.

The Mach number profiles for the planar and axisymmetric hypersonic flow over the same parabola with the same flow conditions are compared in Fig. 10. Notice that the i indexes of the planar results are twice as large as that for the axisymmetric case because twice as many grid points are used in the planar calculations for the same flow geometry. The planar flow field over a wedge has much small Mach numbers behind the shock compared with that of the axisymmetric case. Again, the axisymmetric Mach numbers profiles are much fuller compared to the planar ones. These differences between the planar and axisymmetric boundary layers can affect the stability and transitions of the boundary layers significantly.

Unsteady Flow Solutions

Having obtained the steady flow solutions, the generation of boundary-layer waves by freestream acoustic disturbances is simulated for axisymmetric hypersonic flow over a parabolic cone with a freestream disturbance wave of dimensionless frequency $F = 1770$.

Figure 11 shows the contours for the instantaneous axisymmetric entropy perturbation s' after the unsteady computations are carried out for enough periods in time that periodic solutions have been reached in the entire flow field. The instantaneous contours show the development of a single wave mode in the boundary layer along the surface. The figure also shows a strong effect of the bow shock on the receptivity process. Due to the limit in the length of the computational domain of the present case, only a single mode is developed in the flow field. The mode structure shows a typical characteristics of the shock mode and first mode identified by Refs. [25, 29].

Figures 12 and 13 compare the instability wave structure of the axisymmetric and planar unsteady flows. The figures show that the axisymmetric wave generated in the boundary layer has longer wave length than that of the planar case. The difference in wave lengths may be a result of the difference in Mach numbers behind the shock for the two cases. In addition, the axisymmetric receptivity is also weaker than that of the planar case. The planar flow generates much stronger fluctuations in the wall-normal velocity disturbances. Figure 12 also shows the physical oscillations of the bow shocks due to shock interactions with disturbances from both sides of the shocks.

Figure 14 shows the distribution of instantaneous axisymmetric entropy perturbations along the parabola surface. The disturbance wave growth in this leading edge region is similar to that of the planar case.

Figure 15 shows the contours of the Fourer amplitudes for entropy, horizontal velocity, and the Reynolds stress defined by $\tau = -\overline{\rho u' v'}$. The freestream distur-

bance waves generate strong first-mode wave in the boundary layer along the body surface. The receptivity generates negative Reynolds stress in the leading edge region of the boundary layer and positive Reynolds stress in the downstream region. The growth of the disturbance wave is more clearly shown by the distribution of the Fourier amplitudes of the entropy and Reynolds stress along a ($j = 20$) grid line above the parabola surface (Figs. 16 and 17). Notice that the entropy amplitude increases as x increases though the corresponding Reynolds stress is negative in the leading edge region.

In Refs. [17,25], the dominant disturbance waves generated near the leading edge were identified as the shock mode followed by the first mode and second mode. The change of wave modes as the waves propagate downstream can be shown by the variation of amplitudes of perturbations along grid lines normal to parabola surface at several i grid stations. Figures 18 and 19 show the profiles of $|v'|$ and $|s'|$ amplitudes along the wall-normal directions. The corresponding x coordinates for the grid points on the body surface are given by Table 1. These figures show that as the wave propagates downstream, the structure of the wave modes goes through a gradual conversion to a first mode structure at station $i = 75$. Figure 19 also shows a high gradient region very close to the wall surface in entropy profiles but not in velocity profiles. This thin high gradient layer in the entropy profiles may be the result of inviscid singularity of the entropy wave at the wall in the stagnation point region [30].

The Fourier phase angles of various perturbation variables are useful in understanding the process of wave development in the flow field. Figure 20 shows the contours of the Fourer phase angles for pressure, entropy, and horizontal velocity in the axisymmetric flow field. The smooth increase of pressure phase angles behind the shock shows that the disturbance waves in the region immediately behind the shock are dominated by the forced interaction of the waves with the bow shock. On the other hand, the contours of the pressure phase angles show that in the leading edge region, there is very little pressure phase distortion in the wall-normal direction caused by the effect of the viscous boundary layers. As x increases to further downstream ($x > 0.0$), a viscous layer is developed near the wall which corresponds to the first normal mode of the boundary layers. These results for the compressible boundary layer are similar to the conversion of incompressible unsteady boundary-layer solutions near the leading edge to Tollmien-Schlichting wave solutions of the Orr-Sommerfeld equation further downstream [6].

The contours of the entropy and velocity phase angles in Fig. 20 show much more complex patterns. Figure 21 shows the profiles of entropy phase angles along wall-normal grid lines at several i grid stations. Notice that discontinuities in phase angles in multiples of 360 degs (near $y = 0.03$ in Fig. 20.a) are not genuine discontinuities because of the periodity. These figures show that there is a viscous layer developing in the boundary layer.

For weak monochromatic freestream forcing waves, the generation of instability waves is expected to be linear with respect to the forcing amplitudes for the disturbances with the same fundamental frequency. At the same time, receptivity and stability experiments [22,31] have shown the existence of high harmonics in addition to the linear waves of fundamental frequency. Buter and Reed [12] found nonlinear supersonic harmonic in their incompressible receptivity simulations. Nonlinear higher harmonics are also found in the present DNS studies of axisymmetric receptivity. Figure 22 shows the $Re(s')$ of the entropy disturbances along a grid line above the parabola surface for the fundamental frequency and their second harmonic. Figure 23 shows the entropy disturbance amplitudes along the same grid line for the fundamental mode, mean flow distortion, and second harmonic. The simulations capture the fundamental modes as well as these nonlinear modes.

3-D Unsteady Flow Over A Blunt Wedge

As an example of the application of our new 3-D shock-fitting hypersonic DNS code to blunt wedge, we conduct DNS studies of the receptivity of a three-dimensional boundary layer to weak freestream oblique acoustic disturbance waves for a hypersonic flow boundary layer over a 2-D parabolic leading edge. Though the steady mean flow is 2-D, the unsteady disturbance fields are 3-D because of the oblique freestream waves. The flow conditions are the same as the axisymmetric flow case in the previous section [32]. Figure 24 shows the 3-D shock fitted grids of Zone 1 and Zone 2 resolved by $160 \times 120 \times 16$ and $200 \times 120 \times 16$ grids respectively. The unsteady flow fields are generated by imposing an oblique freestream disturbance at an angle of $\psi = 45°$ with wave amplitude of $\epsilon = 5 \times 10^{-3}$ and $F = 1770$. Figure 25 shows the contours of instantaneous perturbation v' after the flow field reaches a periodic state. The instantaneous contours of v' show the development of 3-D instability waves in the boundary layer on the surface, similar to the first-mode zone. The second mode region is also generated near the end of computational Zone 1. The nonlinear superharmonics in time and in the periodic spanwise direction are analyzed by a Fourier transform of the instantaneous perturbation solutions. Detailed results can be found in [32].

Summary

The receptivity of both axisymmetric and 3-D hypersonic boundary layers to freestream acoustic disturbances has been studied by the DNS of Mach 15 mean flows over a parabolic cone and a parabolic wedge. The full Navier-Stokes equations are solved by using a new explicit 3-D fifth-order shock-fitting upwind scheme and

the Fourier collocation method. The results show that new schemes can resolve 3-D transient hypersonic flow with physical bow-shock oscillations accurately. The receptivity characteristics of axisymmetric and planar hypersonic flow over blunt bodies are studied and compared. Compared with the planar case, the axisymmetric flow over a blunt cone has much high after-shock Mach numbers and much fuller boundary layer profiles. Consequently, the axisymmetric first mode wave generated by the receptivity process has longer wave length and smaller growth rate than the planar case. The simulations are able to generate detailed flow fields information, such as the phase angles and nonliner higher harmonics, which are useful to the understanding of the receptivity process.

Acknowledgments

This research was supported by the Air Force Office of Scientific Research under grant numbers F49620-95-1-0405 and F49620-97-1-0030 monitored by Dr. Len Sakell.

References

[1] Defense Science Board, "Final Report of the Second Defense Science Board Task Force on the National Aero-Space Plane (NASP)," *AD-A274530, 94-00052, November*, 1992.

[2] Reshotko, E., "Boundary Layer Instability, Transition and Control," *AIAA paper 94-0001*, 1996.

[3] Morkovin, M., "On the Many Faces of Transition," *Viscous Drag Reduction*, edited by C. Wells, Plenum, 1969, pp. 1–31.

[4] Goldstein, M. E. and Hultgren, L. S., "Boundary-Layer Receptivity to Long-Wave Free-Stream Disturbances," *Annual Review of Fluid Mechanics*, Vol. 21, pp. 137-166 1989.

[5] Saric, W. S., Reed, H. L., and Kerschen, E. J., "Leading Edge Receptivity to Sound: Experiments, DNS, and Theory," *AIAA Paper 94-2222*, 1994.

[6] Goldstein, **M. E.,** "The evolution of Tollmien-Schlichting **Waves near a** Leading Edge," *Journal of Fluid Mechanics*, **Vol. 127**, pp. 59-81 1983.

[7] Kleiser, L. and **Zang,** T. A., "Numerical Simulation of Transition in Wall-Bounded Shear Flows," *Ann. Rev. Fluid Mech.*, Vol. 23, 1991, pp. 495–535.

[8] Reed, H. L., "Direct Numerical Simulation of Transition: the Spatial Approach," *Progress in Transition Modeling*, AGARD-Report-793 1994.

[9] Pruett, C. D., Zang, T. A., Chang, C.-L., and Carpenter, M. H., "Spatial Direct Numerical Simulation of High-Speed Boundary-Layer Flows, Part I: Algorithmic Considerations and Validation," *Theoretical and Computational Fluid Dynamics*, Vol. 7, 1995, pp. 49–76.

[10] Murdock, J. W., "Tollmien-Schlichting Waves Generated by Unsteady Flow over Parabolic Cylinders," *AIAA paper 81-0199*, 1981.

[11] Lin, N., Reed, H. L., and Saric, W. S., "Effect of Leading-Edge Geometry on Boundary-Layer Receptivity to Freestream Sound," *Instability, Transition, and Turbulence*, Vol. M. Y. Hussaini et al., editors, pp. 421-440, Springer-Verlag, 1992.

[12] Buter, T. A. and Reed, H. L., "Boundary Layer Receptivity to Free-Stream Vorticity," *Physics of Fluids*, Vol. 6, No. 10, 1994, pp. 3368–3379.

[13] Casalis, G. and Cantaloube, B., "Receptivity by Direct Numerical Simulation," *Direct and Large-Eddy Simulation I*, Vol. P. R. Voke et al., editors, pp. 237-248, Kluwer Academic Publishers, 1994.

[14] Collis, S. S. and Lele, S. K., "A Computational Approach to Swept Leading-Edge Receptivity," *AIAA paper 96-0180*, 1996.

[15] Corke, T. C. and Haddad, O., "Receptivity to sound on a parabolic leading edge," *In Transitional Boundary Layers in Aeronautics*, Vol. Edited by R.A.W.M. Henkes and J. L. van Ingen, pp. 403-412, North-Holland, Amsterdam, 1996.

[16] Liu, Z., Xiong, G., and Liu, C., "Receptivity to Freestream Vortical Disturbance of 2D and 3D Airfoils," *AIAA paper 96-2084*, January 1996.

[17] Zhong, X., "Direct Numerical Simulation of Hypersonic Boundary-Layer Transition Over Blunt Leading Edges, Part II: Receptivity to Sound (Invited)," *AIAA paper 97-0756*, January 1997.

[18] Reshotko, E., "Hypersonic Stability and Transition," *in Hypersonic Flows for Reentry Problems, Eds. J.-A. Desideri, R. Glowinski, and J. Periaux, Springer-Verlag*, Vol. 1, 1991, pp. 18–34.

[19] Morkovin, M. V., "Transition at Hypersonic Speeds," *ICASE Interim Report 1*, Vol. NASA CR 178315, May, 1987.

[20] Reshotko, E. and Khan, N. M. S., "Stability of the Laminar Boundary Layer on a Blunt Plate in Supersonic Flow," *IUTAM Symposium on Laminar-Turbulent Transition*, edited by R. Eppler and H. Fasel, Springer-Verlag, Berlin, 1980, pp. 186–190.

[21] Kendall, J. M., "Wind Tunnel Experiments Relating to Supersonic and Hypersonic Boundary-Layer Transition," *AIAA Journal*, Vol. Vol. 13, No. 3, pp. 290–299, 1975.

[22] Stetson, K. F. and Kimmel, R. L., "On Hypersonic Boundary Layer Stability," *AIAA paper 92-0737*, 1992.

[23] Lee, T. K. and Zhong, X., "Spurious Numerical Oscillations in Numerical Simulation of Supersonic Flows Using Shock Capturing Schemes," *AIAA paper 98-0115*, January 1998.

[24] Zhong, X., "Direct Numerical Simulation of Hypersonic Boundary-Layer Transition Over Blunt Leading Edges, Part I: New Numerical Methods and Validation (Invited)," *AIAA paper 97-0755, 35th AIAA Aerospace Sciences Meeting and Exhibit, January 6-9, Reno, Nevada*, 1997.

[25] Hu, S. H. and Zhong, X., "Linear Stability of Compressible Couette Flow," *AIAA paper 97-0432*, January 1997.

[26] Mack, L. M., "Boundary Layer Linear Stability Theory," *AGARD report, No. 709*, 1984, pp. 3–1 to 3–81.

[27] Williamson, J. H., "Low-Storage Runge-Kutta Schemes," *Journal of Computational Physics*, Vol. 35, 1980, pp. 48–56.

[28] Lees, L. and Lin, C. C., "Investigation of the Stability of the Laminar Boundary Layer in Compressible Fluid," *NACA TN No. 1115*, 1946.

[29] Hu, S. and Zhong, X., "Hypersonic Boundary-Layer Stability over Blunt Leading Edge with Bow-Shock Effects," *AIAA paper 98-0433*, January 1998.

[30] Zhong, X., Joubert, X., and Lee, T. K., "The Interaction of Freestream Disturbances and the Bow Shock in Hypersonic Flow Past a Cylinder," 1995, Presented in 20th International Symp. on Shock Waves, July 23-28, 1995, Pasadena, California.

[31] Dietz, A., "Distributed Boundary Layer Receptivity to Convected Vorticity," *AIAA paper 96-2083*, June 1996.

[32] Zhong, X., "DNS of Boundary-Layer Receptivity to Freestream Sound for 3-D Hypersonic Flows Over Blunt Wedges and Cones," *In proceeding of First AFOSR International Conference on Direct Numerical Simulation and Large Eddy Simulation, August 1997, Ruston, LA*, 1997.

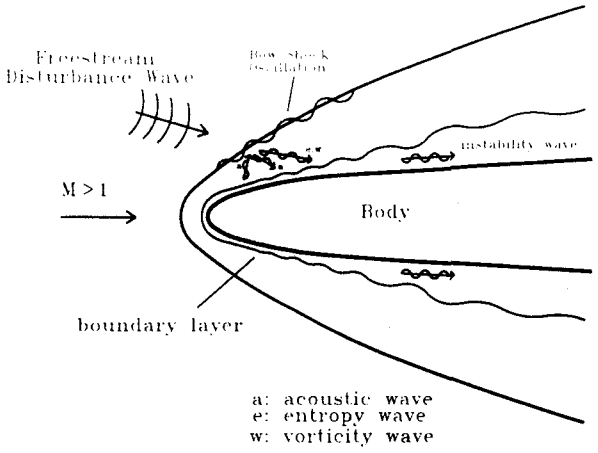

Figure 1: A schematic of the receptivity wave field of the interaction between the bow shock and free-stream disturbances.

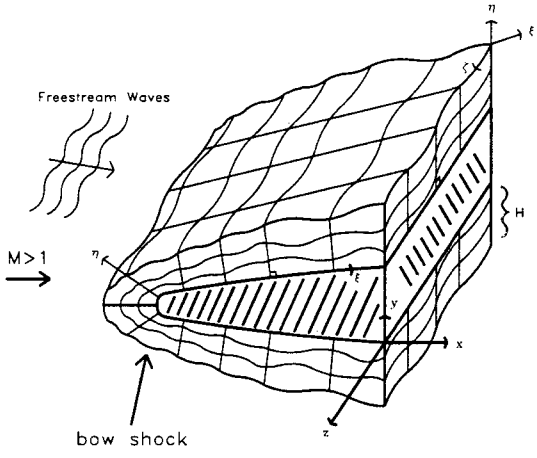

Figure 2: A schematic of 3-D shock fitted grids for the DNS of hypersonic boundary-layer receptivity to freestream disturbances over a blunt leading edge.

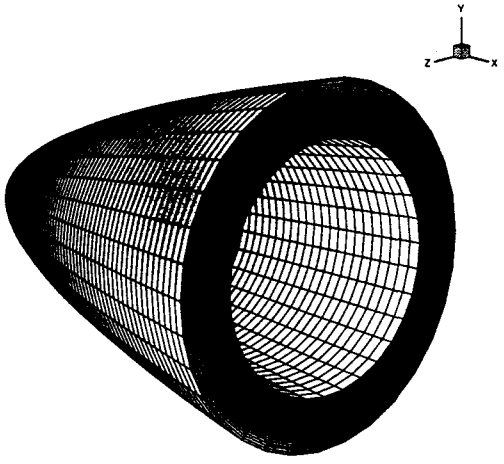

Figure 3: Computational grid for the DNS of the receptivity of a 3-D hypersonic boundary layer over a blunt cone.

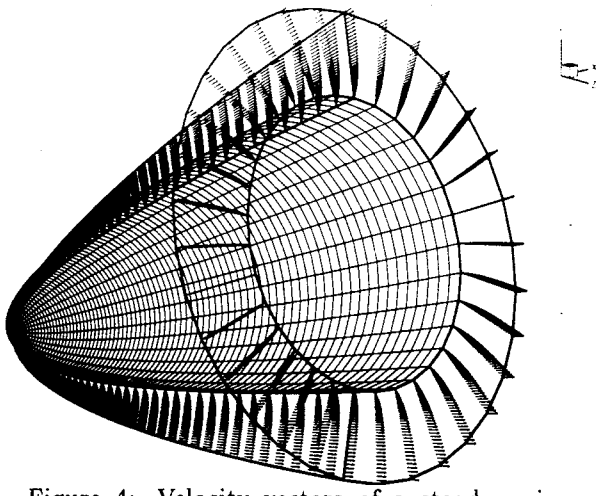

Figure 4: Velocity vectors of a steady axisymmetric Mach 15 viscous hypersonic flow over a blunt cone.

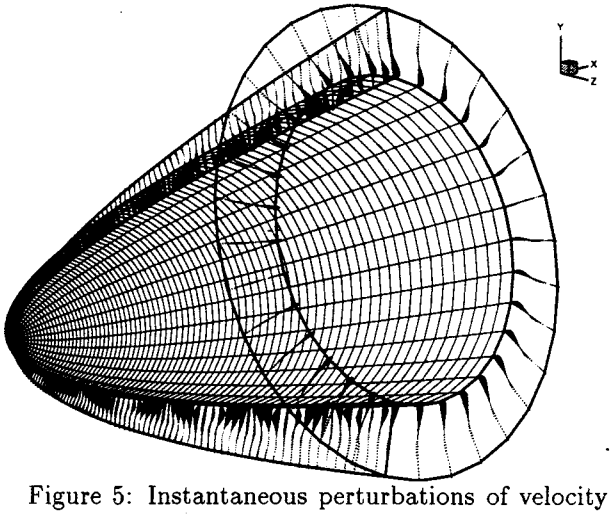

Figure 5: Instantaneous perturbations of velocity vectors for the DNS of receptivity to freestream sound for a Mach 15 hypersonic flow over a blunt cone ($F = 1770$).

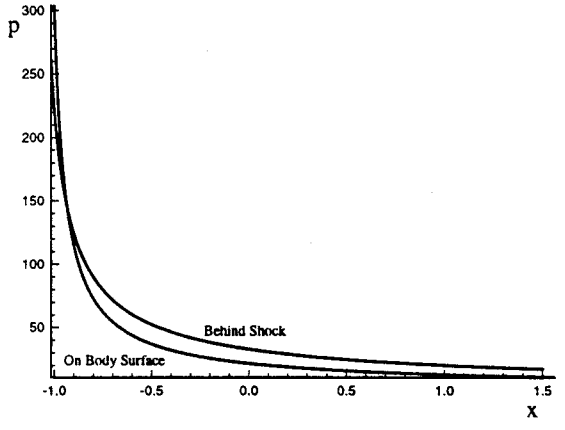

Figure 6: Variation of axisymmetric steady base flow pressure along the parabola surface and behind the bow shock.

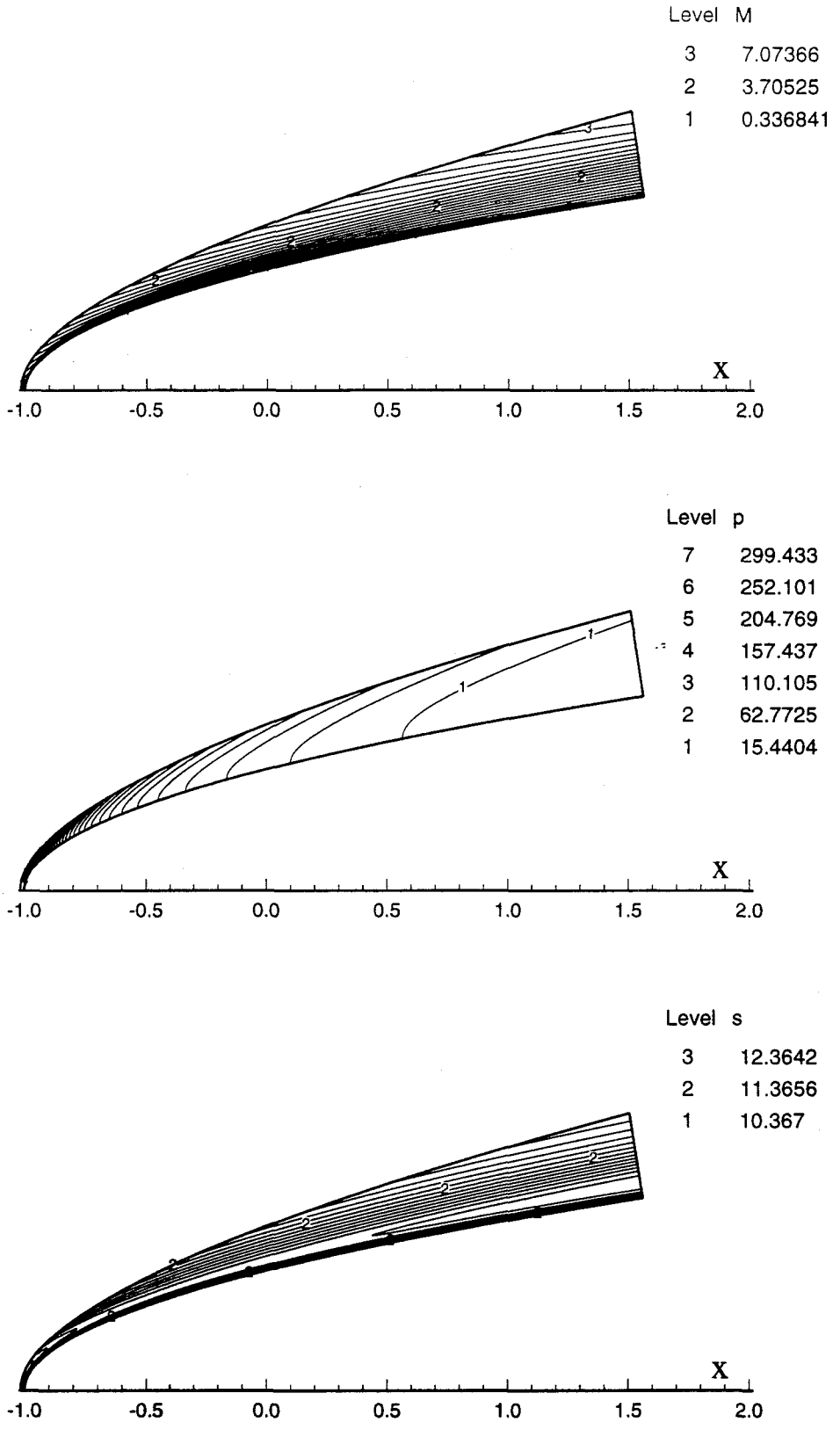

Figure 7: Contours of axisymmetric steady base flow solutions behind the bow shock: Mach numbers (upper figure), pressure (middle figure), and entropy (lower figure).

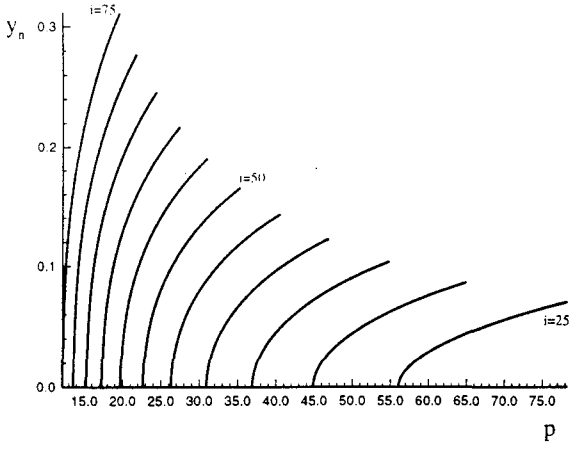

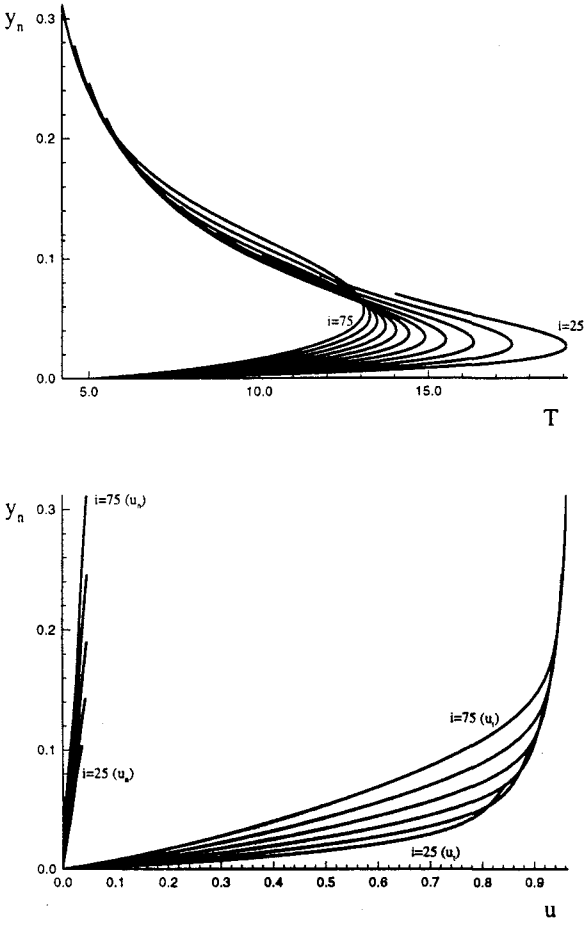

Figure 8: Profiles of axisymmetric steady flow variables along a range of wall-normal grid lines at several i grid stations: pressure (upper figure), temperature (middle figure), and tangential and normal velocities (lower figure).

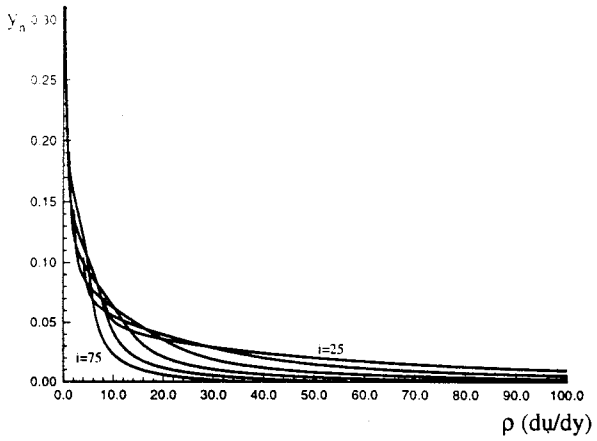

Figure 9: Variation of steady $\rho(du_t/dy_n)$ related to the generalized inflection point for the axisymmetric steady flow variables along a range of wall-normal grid lines at several i grid stations.

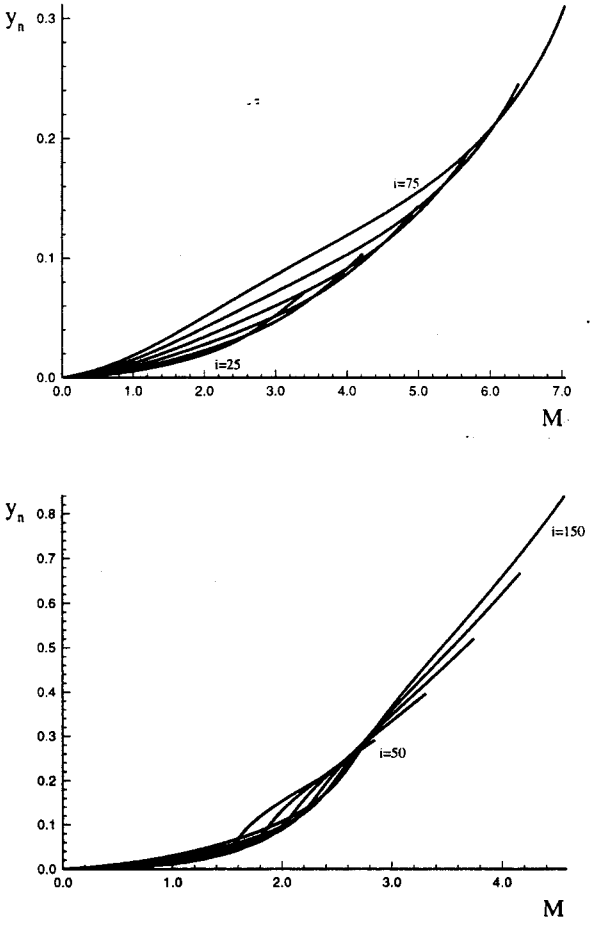

Figure 10: Comparison of planar and axisymmetric Mach number profiles along wall-normal grid lines at several i grid stations: planar 2-D case (upper figure) and axisymmetric case (lower figure).

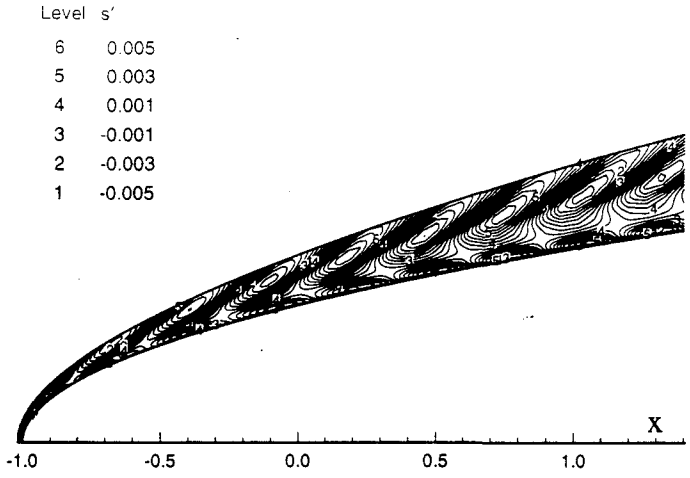

Figure 11: Instantaneous axisymmetric entropy perturbation contours generated by the receptivity to a freestream acoustic wave by hypersonic flow over a cone ($F = 1770$).

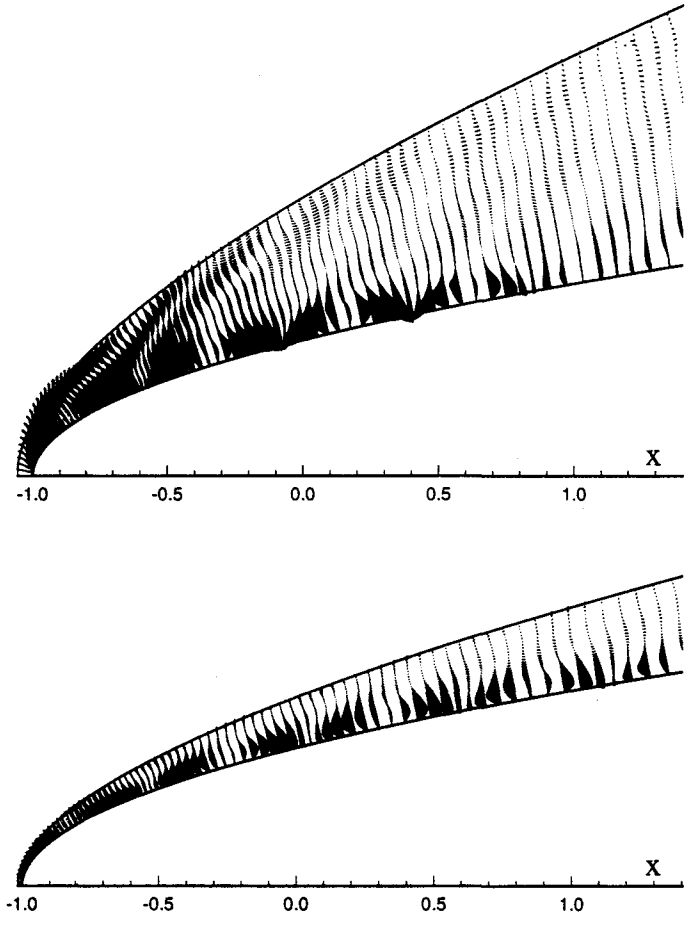

Figure 12: Comparison of planar and axisymmetric instantaneous perturbation velocity vector contours for the case of $F = 1770$: planar flow (upper figure) and axisymmetric flow (lower figure).

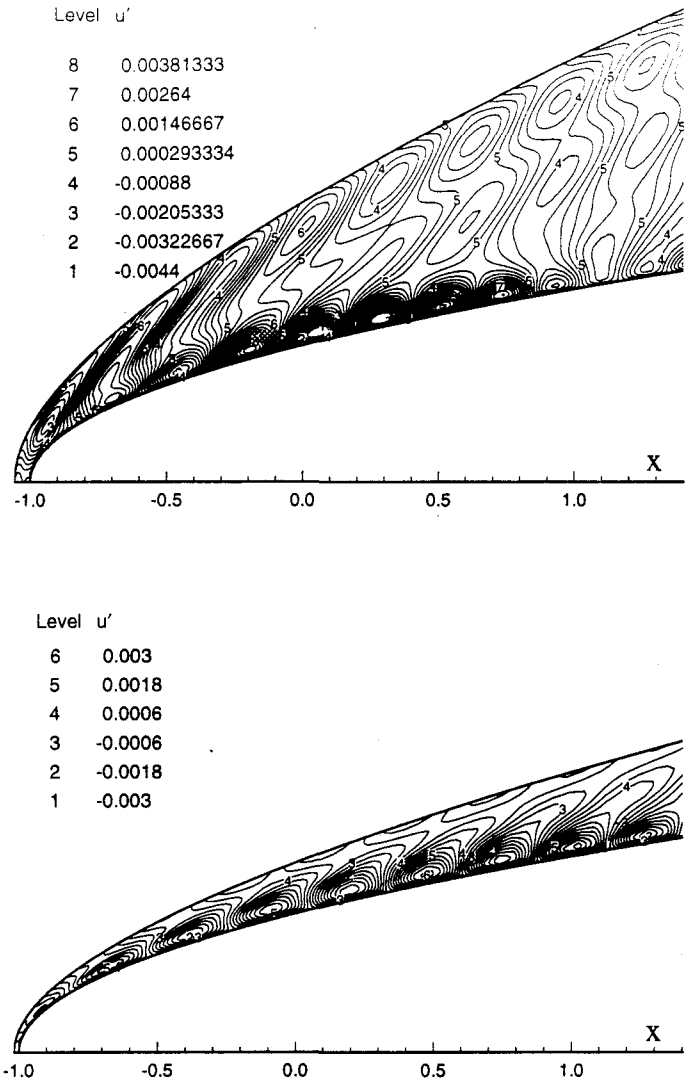

Figure 13: Comparison of planar and axisymmetric instantaneous perturbation velocity u' contours for the case of $F = 1770$: planar flow (upper figure) and axisymmetric flow (lower figure).

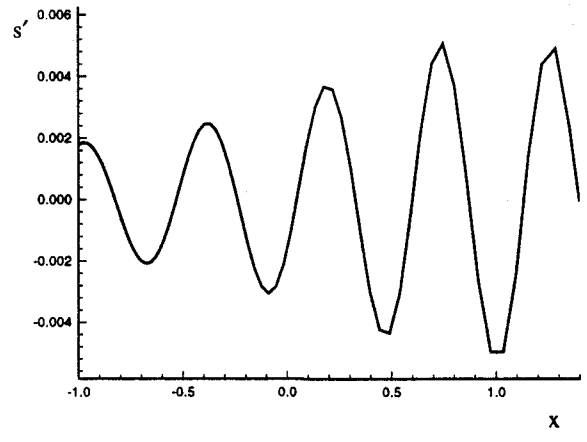

Figure 14: Distribution of instantaneous axisymmetric entropy perturbations along the parabola surface ($F = 1770$).

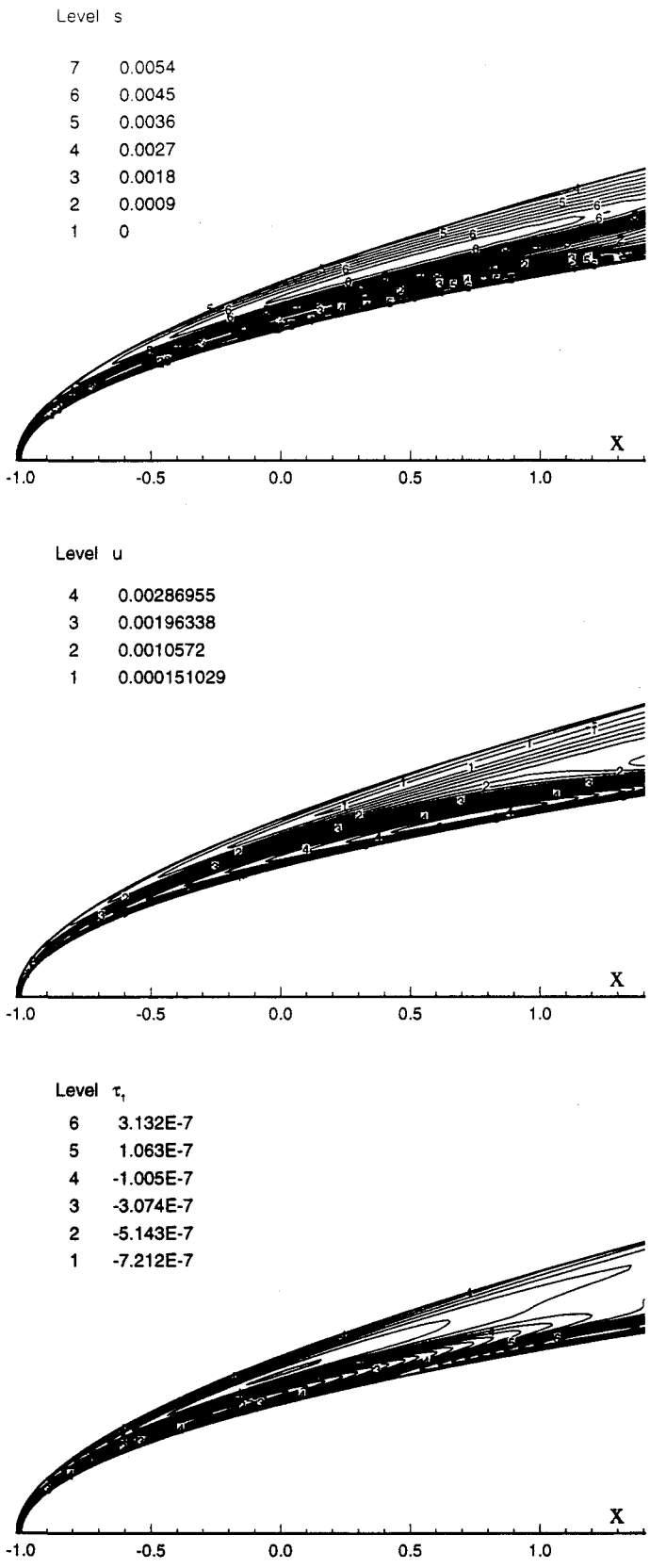

Figure 15: Fourier amplitude contours of perturbation variables for the axisymmetric flow of $F = 1770$: entropy $|s'|$ (upper figure), horizontal velocity $|u'|$ (middle figure), and Reynolds stress $\tau = -\overline{\rho u' v'}$ (lower figure).

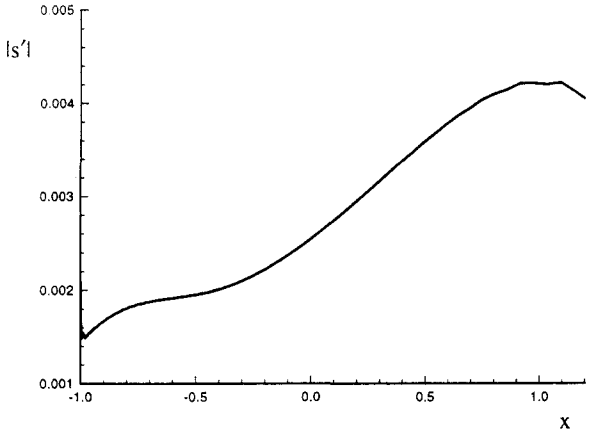

Figure 16: Distribution of the axisymmetric entropy Fourier amplitudes along a ($j = 20$) grid line above the parabola surface ($F = 1770$).

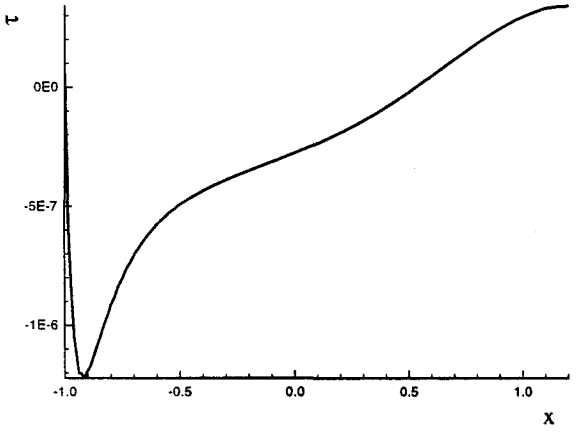

Figure 17: Distribution of the axisymmetric Reynolds Stress ($\tau = -\overline{\rho u' v'}$) along a ($j = 20$) grid line above the parabola surface ($F = 1770$).

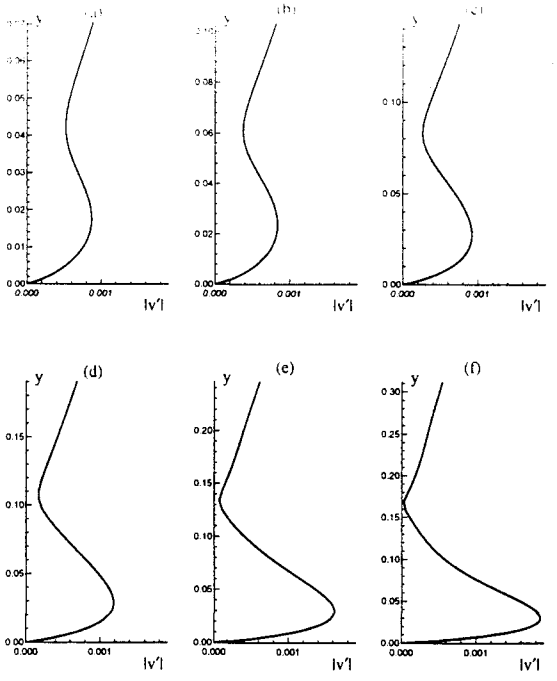

Figure 18: Profiles of amplitudes of axisymmetric vertical velocity $|v'|$ perturbations along wall-normal grid lines at several i grid stations: (a) $i = 25$, (b) $i = 35$, (c) $i = 45$, (d) $i = 55$, (e) $i = 65$, and (f) $i = 75$.

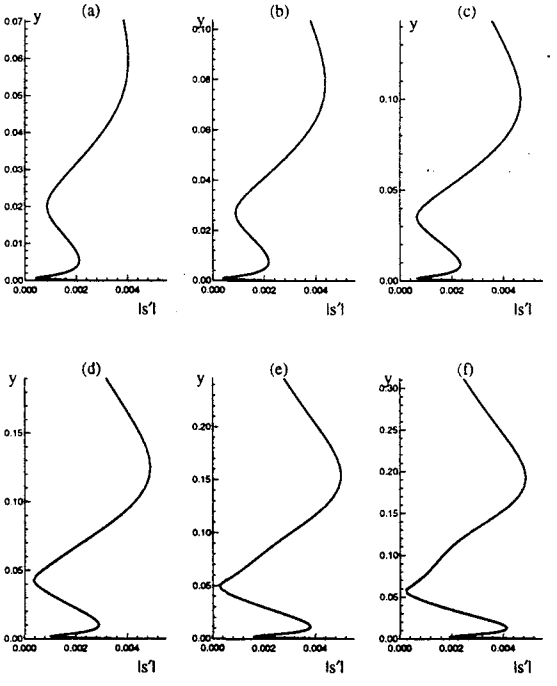

Figure 19: Profiles of amplitudes of axisymmetric entropy $|s'|$ perturbations along wall-normal grid lines at several i grid stations.

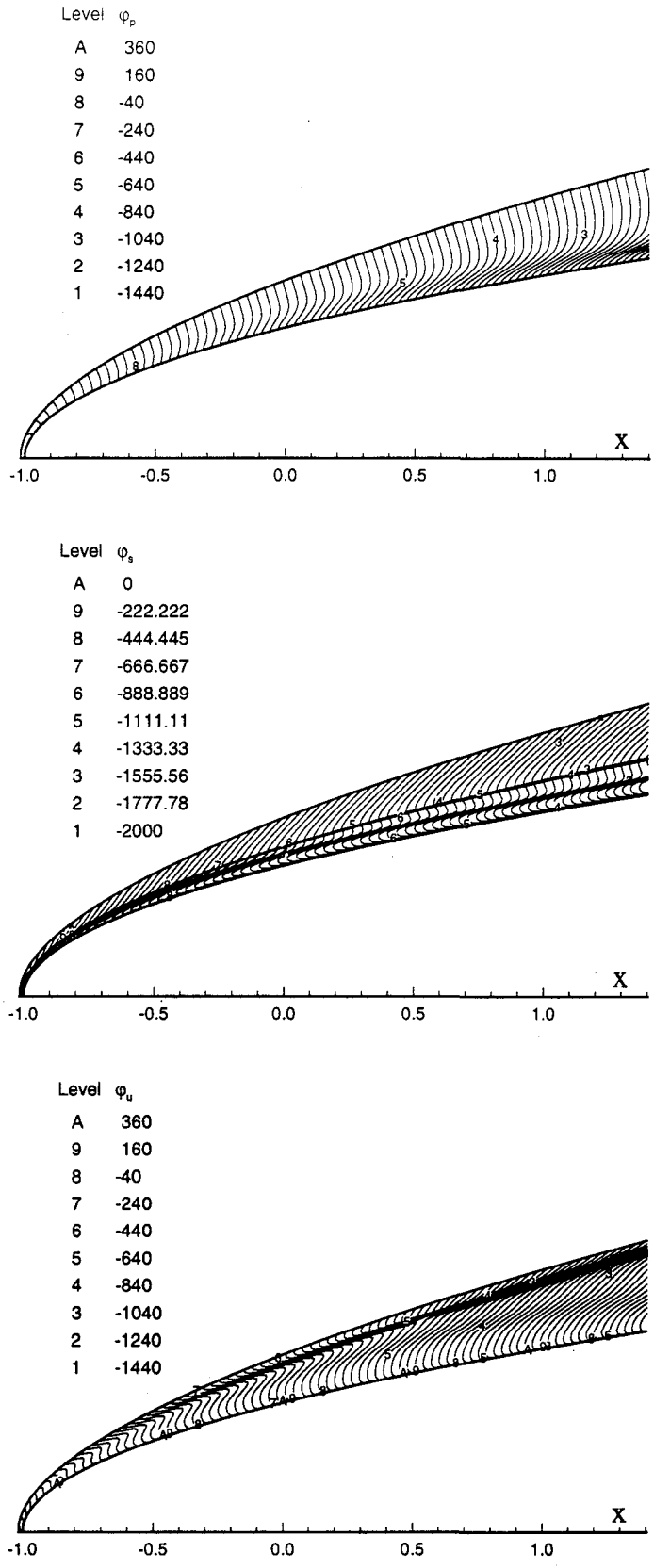

Figure 20: Contours of Fourier phase angles (in degrees) of perturbation variables for the axisymmetric flow of $F = 1770$: pressure φ_p (upper figure), entropy φ_s (middle figure), and horizontal velocity φ_u (lower figure).

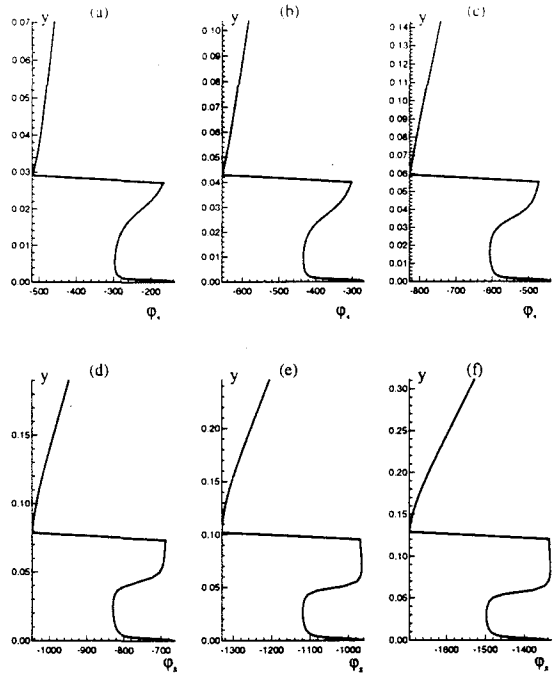

Figure 21: Profiles of axisymmetric entropy $|s'|$ perturbations phase angles (in degrees) along wall-normal grid lines at several i grid stations.

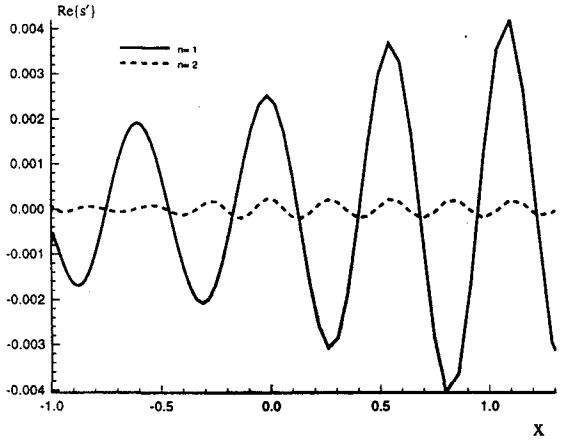

Figure 22: Distribution of the real part of axisymmetric entropy perturbation $Re(s')$ for the fundamental mode ($n = 1$) and the nonlinear second harmonic ($n = 2$) along a ($j = 20$) grid line above the parabola surface. The magnitude of the second harmonic is amplified 10 times in figures.

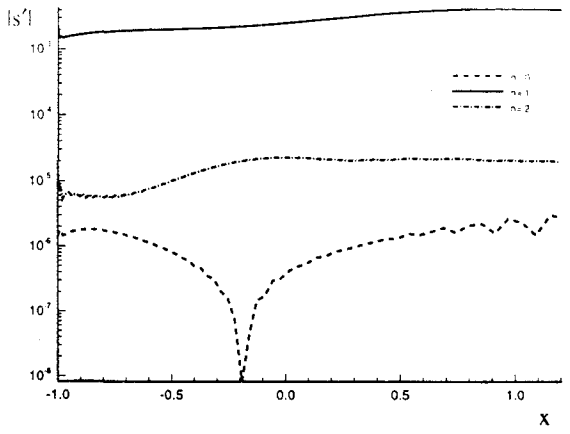

Figure 23: Axisymmetric entropy perturbation amplitudes for the fundamental mode ($n = 1$), second harmonic ($n = 2$), and mean flow distortion ($n = 0$) along a ($j = 20$) grid line above the parabola surface.

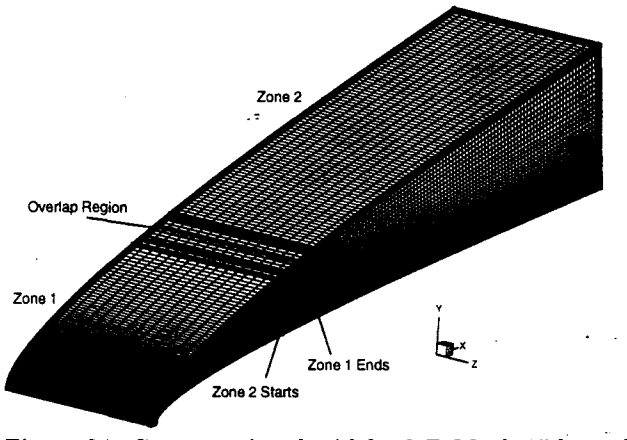

Figure 24: Computational grid for 3-D Mach 15 boundary layer receptivity to freestream oblique disturbance waves for the case of parabolic wedge.

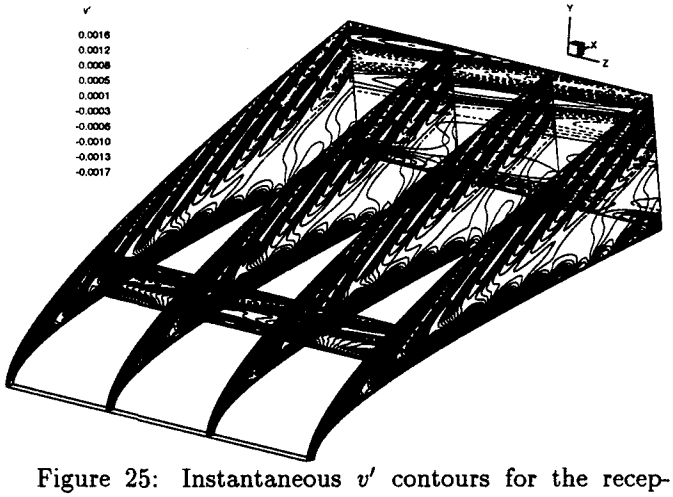

Figure 25: Instantaneous v' contours for the receptivity to freestream disturbances for 3-D hypersonic boundary-layer over a parabolic wedge ($F = 1770$).